Journal of
Synchrotron
Radiation

ISSN 0909-0495

Received 31 May 2012
Accepted 13 September 2012

Accounting for low-frequency synchrotron X-ray beam position fluctuations for dynamic visualizations

J. Hinebaugh, P. R. Challa and A. Bazylak*

Mechanical and Industrial Engineering, Faculty of Applied Science and Engineering, University of Toronto, 5 King's College Road, Toronto, ON, Canada M5S 3G8. E-mail: abazylak@mie.utoronto.ca

Synchrotron X-ray radiography on beamline 05B1-1 at the Canadian Light Source Inc. was employed to study dynamic liquid water transport in the porous electrode materials of polymer electrolyte membrane fuel cells. Dynamic liquid water distributions were quantified for each radiograph in a sequence, and non-physical liquid water measurements were obtained. It was determined that the position of the beam oscillated vertically with an amplitude of $\sim$25 μm at the sample and a frequency of $\sim$50 mHz. In addition, the mean beam position moved linearly in the vertical direction at a rate of 0.74 μm s^{-1}. No evidence of horizontal oscillations was detected. In this work a technique is presented to account for the temporal and spatial dependence of synchrotron beam intensity, which resulted in a significant reduction in false water thickness. This work provides valuable insight into the treatment of radiographic time-series for capturing dynamic processes from synchrotron radiation.

Keywords: synchrotron radiography; fluctuations; beam movement; fuel cells; polymer electrolyte membrane fuel cells; 05B1-1 beamline.

1. Introduction

Synchrotron-based X-ray radiography is advantageous for providing almost parallel monochromatic beams with high intensities (10^{11}–10^{15} photons s^{-1} cm^{-2}) to obtain radiographs with high temporal (up to 0.8 s per frame) and spatial (up to 1 μm per pixel) resolutions (Hartnig & Manke, 2009). It has been recently employed by a number of researchers to investigate the evolution and distribution of liquid water in the porous components of polymer electrolyte membrane fuel cells (PEMFCs) (Hartnig *et al.*, 2009; Markoetter *et al.*, 2011; Kuhn *et al.*, 2011; Krüger *et al.*, 2011; Manke *et al.*, 2007; Maier *et al.*, 2010; Lee *et al.*, 2010; Schneider *et al.*, 2010). Readers are referred to a review provided by Bazylak (2009) for a thorough overview of the various techniques that have been recently employed to visualize PEMFCs. Using synchrotron radiography, the visualization of dynamic liquid water behaviour in PEMFC materials can be achieved with a time series of radiographs, where the change of liquid water content between two radiographs can be quantified, assuming that the beam characteristics remain constant. However, Chattopadhyay (1990) reported that synchrotron-generated beam instabilities exist on time scales ranging from 10^{-9} to 10^{9} s. For synchrotron-based X-ray radiography of liquid water in PEMFC materials, where temporal resolutions are on the order of 1 s per frame and experiments may last from several minutes to an hour, X-ray beam instabilities with time scales between 10^{-1} to 10^{4} s may cause artefacts. Such instabilities may be the result of mechanical vibrations, ground motion, cooling water temperature fluctuations, electric power cycles or atmospheric temperature cycles (Chattopadhyay, 1990). Additionally, a diffraction-based monochromator can be employed to select a narrow bandwidth of X-ray energies for imaging purposes. The high-intensity polychromatic light bombarding the initial monochromater crystal can create thermal distortions of the crystal, generating instabilities (Leonard *et al.*, 2008) and affecting the vertical beam position (Chumakov *et al.*, 2004; Proux *et al.*, 2006). In this paper we report on the observed time-dependent fluctuations in the beam position that is manifested in obtained radiographs of dynamic liquid water generation in PEMFC materials, and we present a technique that reduces the effect of these fluctuations while enabling the quantification of water content.

2. Imaging set-up

The analysis presented in this paper is based on X-ray absorption radiograph sequences collected from PEMFC experiments at the BioMedical Imaging and Therapy Bending Magnet (05B1-1) beamline at the Canadian Light Source Inc. (CLS) synchrotron. The 05B1-1 beamline consists of a bending-magnet source followed by masks, collimators, shutters, slits, filters and a double-crystal Bragg monochromator at

13 m from the source (Belev *et al.*, 2011; Wysokinski *et al.*, 2007). The samples are placed at a distance of ∼25 m from the source. Absorption radiographs are obtained with a Hamamatsu C9300-124 (12-bit, 10 Megapixel) CCD camera at 10–50 cm from the sample. A 2010 CLS Research Report (Dalzel, 2010) listed storage ring beam stability to ∼1 µm vertically and a few micrometres horizontally.

The chosen optical equipment and camera settings (exposure and gain) provided an exposure time of 0.9 s and pixel size of 4.5 µm. The photon energy was set to either 23 or 25 keV depending on the experiment. The optical set-up was rated to yield a spatial resolution of 10 µm; however, positions of sharp features in the radiographs could only be determined with an accuracy of 20 µm. Therefore, from the radiographs, it was not possible to confirm a spatial resolution of 10 µm.

3. Experiments

The experiments enable the visualization of liquid water in the gas diffusion layer (GDL) of a PEMFC. The GDL is a planar, porous component of the PEMFC that often becomes saturated with liquid water during operation, affecting performance.

Two experiments will be closely examined in this work to isolate the behaviour of the synchrotron X-ray beam: (*a*) an *in situ* study of through-plane water distribution in the GDL of a PEMFC, and (*b*) an *ex situ* study of through-plane water distribution in a PEMFC GDL. Fig. 1(*a*) schematically shows the *in situ* experimental set-up and Fig. 1(*b*) shows a typical raw radiograph. In the *ex situ* study, liquid water was injected into GDLs compressed in a sample holder. Fig. 2(*a*) schematically shows the *ex situ* sample holder and Fig. 2(*b*) shows a typical raw radiograph. While both studies are oriented such that the plane of the GDL material is parallel to the X-ray beam, the *in situ* study was vertically oriented while the *ex situ* study was horizontal.

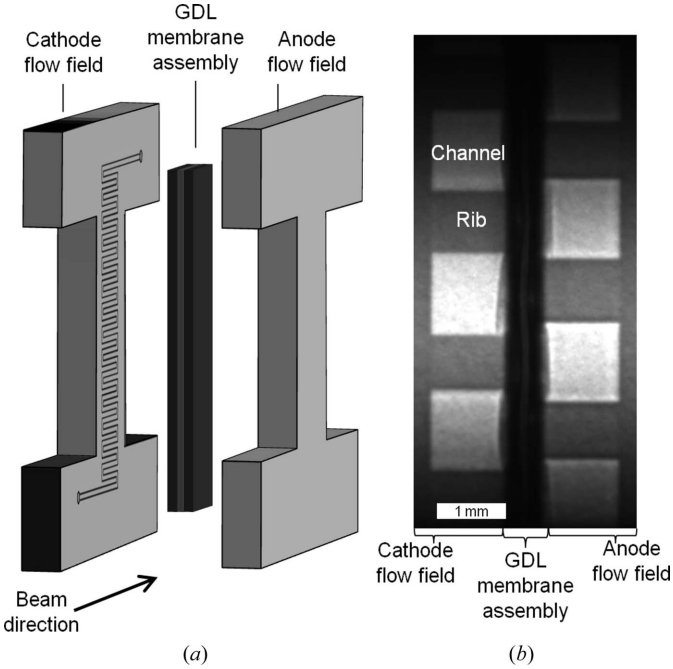

Figure 1
Exploded view of fuel cell components and relative beam direction for *in situ* experiment (*a*). Example radiograph of *in situ* experiment (*b*).

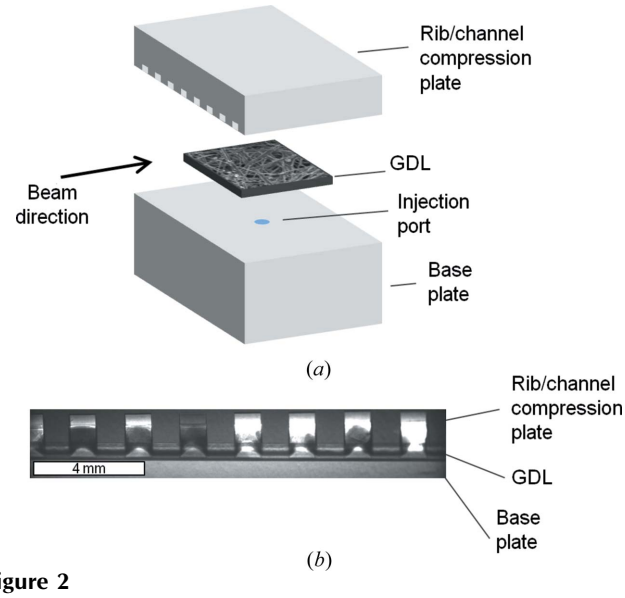

Figure 2
Exploded view of injection apparatus components and relative beam direction for *ex situ* experiment (*a*). Example radiograph of *ex situ* experiment (*b*).

Radiographs are collected at 0.9 s per frame over a period of time to enable the visualization of dynamic water invasion processes. Imaging was initiated while materials were in a 'dry' state, containing little to no liquid water, for 2–15 min. Imaging continued through the 'wet' state, where liquid water entered the GDL. Water content in the GDL was calculated by normalizing wet-state radiographs to dry-state radiographs using the techniques described in the following section.

Although Schneider *et al.* (2010) observed that the performance of a fuel cell decreased after minutes of exposure to synchrotron radiation, it has to be noted that the performance drop was only observed when the entire active area of a fuel cell was exposed to synchrotron radiation. In the experiments described in this paper, the entire active area of the fuel cell was not exposed to synchrotron radiation. However, the local effects on the components of the GDL and the PEMFC that were exposed to synchrotron radiation are, as of yet, unknown.

4. Beer–Lambert image analysis

The Beer–Lambert law relates the attenuated intensity with the incident intensity and the thickness of a single material in the path of an X-ray beam as (Lee *et al.*, 2010)

$$I = I_0 \exp(-\mu X), \tag{1}$$

where I is the attenuated intensity, I_0 is the incident intensity of the beam, μ is the attenuation coefficient of the material with respect to the beam energy, and X is the material thick-

ness. The intensity of the beam upon passing through the multi-component sample in the dry state is given by

$$I_{\rm dry} = I_0 \exp\left(-\sum \mu_i X_i\right), \quad (2)$$

where μ_i is the material attenuation coefficient, X_i is the material thickness traversed by the beam, and $i = 1 \ldots n$, where n is the number of materials in the path of the beam. Similarly, the intensity of the beam that passes through the sample in the wet state at time t is given by

$$I_{{\rm wet},t} = I_0 \exp\left[-\left(\mu_{\rm water} X_{{\rm water},t} + \sum \mu_i X_i\right)\right], \quad (3)$$

where $\mu_{\rm water}$ is the attenuation coefficient of the water and $X_{{\rm water},t}$ is the thickness of water with respect to the beam direction at time t. From equations (2) and (3), the following expression is obtained for water thickness, $X_{{\rm water},t}$, in the GDL with respect to dry-state and wet-state intensity values,

$$X_{{\rm water},t} = -\left[\log(I_{{\rm wet},t}/I_{\rm dry})/\mu_{\rm water}\right]. \quad (4)$$

In this manner, raw wet-state radiographs can be normalized to raw dry-state radiographs. Equation (4) is employed with the assumption that I_0 remains constant with respect to time, allowing it to be removed when combining (2) and (3). When the incident beam changes intensity or position, this leads to the calculation of a non-physical addition or removal of liquid water from the system. Likewise, false water signals can result from material movement during an experiment as X_i is also assumed to remain constant for all materials other than water, since the fuel cell apparatus does not contain moving parts. While material movement must be minimized by experimental design, the following sections discuss the steps taken to account for variations in the intensity and position of the incident beam.

5. Ring current decay

Synchrotron light is an emission resulting from the radial acceleration of electrons travelling at near-light speeds. Synchrotron facilities maintain a high-speed beam of electrons in a storage ring, and the emitted light intensity is a function of several factors, including the number of electrons contained in the ring. The electron beam within the storage ring at a synchrotron facility naturally decreases in current over time and must be replenished periodically. At the CLS this decrease in ring current and subsequent light intensity degradation can be assumed to be linear over short time periods, causing a linear decrease in image intensity. To account for this linear intensity decrease, subsequent images from the first captured image are corrected *via* the following equation,

$$I_{t,{\rm corr}} = I_t(C_0/C_t), \quad (5)$$

where $I_{t,{\rm corr}}$ represents the corrected intensity, I_t is the measured intensity, and C_t represents the ring current at time t. C_0 represents the ring current at a reference time, $t = 0$.

6. Beam position movement

When the obtained radiographs from both the *ex situ* and *in situ* experiments were originally analyzed prior to our observation of beam oscillations, we observed unrealistic water thickness values (Fig. 3*a*) when using a reference dry-state radiograph at time $t = 0$. After normalization, non-negligible water thickness values (±350 µm) were observed in regions that were physically constrained and had no access to liquid water, such as the solid graphite or polycarbonate components of the apparatuses. Therefore, it was determined that either the illumination source or the imaging system was causing the artefacts. Most originally normalized radiographs in any given sequence were afflicted to some degree by these artefacts; however, periodically, some normalized radiographs exhibited minimal artefacts (Fig. 3*b*). Such periodic artefacts could be explained with X-ray beam position oscillation.

The incident X-ray beam at the 05B1-1 line has the dimensions 240 mm (horizontal direction) by 7 mm (vertical direction) at the sample location, with the peak intensity, or 'hotspot', near the centre horizontal axis. If the beam position should rise in the vertical direction, for example, the associated hotspot would also rise, leading to a brightening of the image above the original hotspot position and a darkening of the image below the original hotspot position. From Fig. 3(*a*) it can be seen that the artefacts were nearly uniform along the horizontal dimension but were a strong function of vertical position. Additionally, the artefact severity appeared to fluctuate over time.

To demonstrate these fluctuations, average intensity levels from the two positions outlined in Fig. 4(*a*) are calculated over a period of 3 min and displayed in Fig. 4(*b*). Regions 1 and 2 are within the graphite block (non-porous component), which is immobile and inaccessible to liquid water. As can be seen from Fig. 4(*a*), these regions are located above and below the

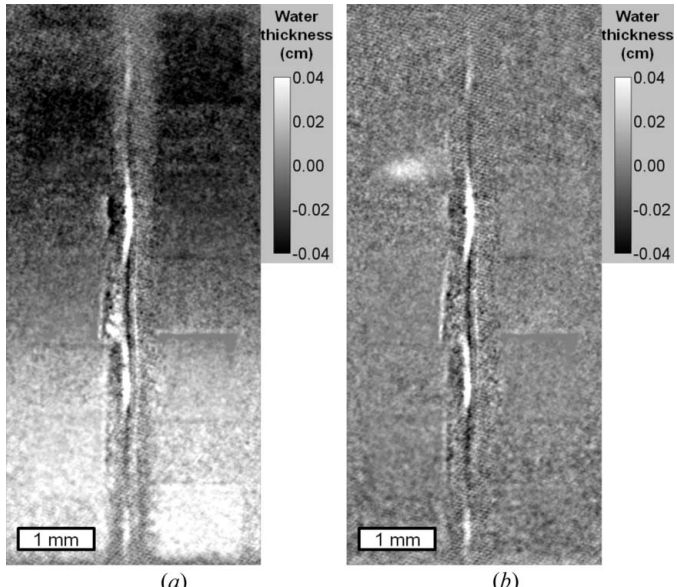

(*a*) (*b*)

Figure 3
Radiographs normalized to the first dry-state image in the sequence demonstrating the presence of high levels of artefacts appearing at some points in time (*a*), and little to no artefacts are present at others (*b*).

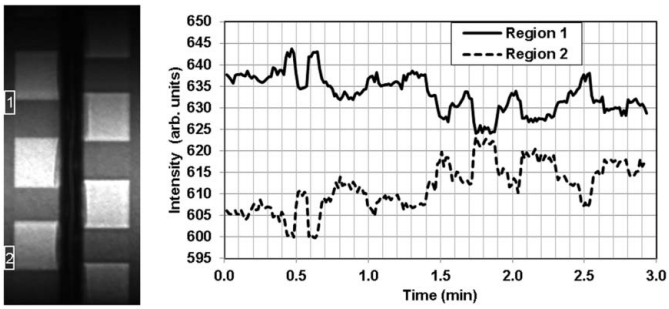

(*a*) (*b*)

Figure 4
Raw radiograph (*a*) with two regions (highlighted) selected on either side of the vertical hotspot position where the mean intensity value is to be calculated. Mean intensity values for regions 1 and 2 over time (*b*).

vertical position of the hotspot. In the absence of beam position movement, the intensity should be constant over time. Instead, it can be seen that the intensity values fluctuate (Fig. 4*b*). Region 2 exhibits an inverted intensity pattern compared with region 1. Specifically, at time *t*, when the intensity of region 1 is increasing, the intensity of region 2 is decreasing. This result is consistent with the predicted behaviour of vertical beam position movement described above.

To identify the existence of significant horizontal beam position movement, the intensity data collected during the horizontally oriented *ex situ* experiment is examined. As can be seen from Fig. 5(*a*), regions 1 and 2 are located to the left and right of the horizontal position of the hotspot. In the absence of beam position movement, the intensity should be constant over time. Instead, it can be seen that the intensity values fluctuate (Fig. 5*b*). These regions exhibit the same fluctuations. Specifically, at time *t*, when the intensity of region 1 is increasing, the intensity of region 2 is also increasing. Analogous to the predicted behaviour of vertical beam position movement, horizontal beam position movement would create inverted intensity patterns. Since this is not the case in Fig. 5, horizontal beam position movement is considered negligible. It should be noted that, for clarity, region 1 was selected with a shorter radial distance to the hotspot compared with region 2 in order to create an offset in the intensity values.

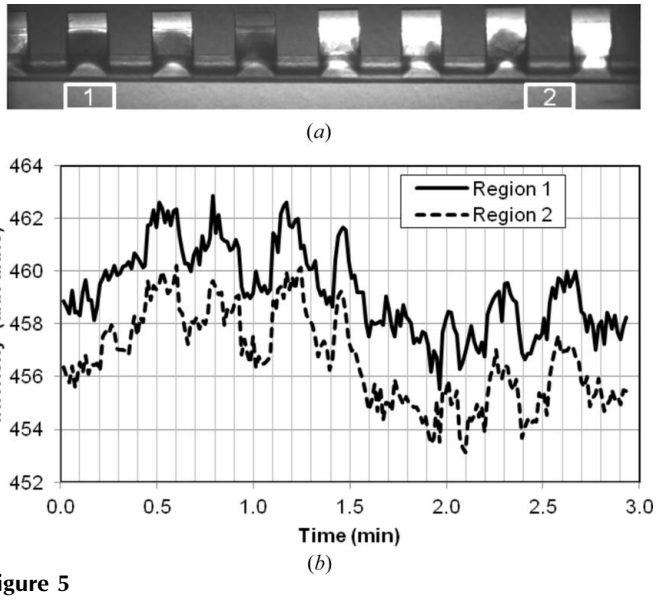

(*a*) (*b*)

Figure 5
Raw radiograph (*a*) with two regions (highlighted) selected on either side of the horizontal hotspot position where the mean intensity value is to be calculated. Mean intensity values for regions 1 and 2 over time (*b*).

A homogeneous section of the *in situ* experimental apparatus that was free of water during the entirety of the visualization was chosen to examine the behaviour of the beam hotspot position (highlighted in Fig. 6*a*). The vertical intensity profile is measured [black line in Fig. 6(*b*)], and an eighth-order polynomial is fit to the intensity profile of each frame [red line in Fig. 6(*b*)], and the peak of the polynomial is assumed to represent the vertical position of the beam hotspot. The peak is calculated for each frame over a period of 3 min and displayed in Fig. 6(*c*). Oscillatory features of the peak position are present with a period of approximately 20 s and a range of vertical positions spanning 50 µm. Over an extended period of time (shown in Fig. 6*d*) another trend is seen in the vertical hotspot position behaviour, where a linear fit of the data reveals that the average hotspot position moves vertically at a rate of 0.74 µm min^{-1}.

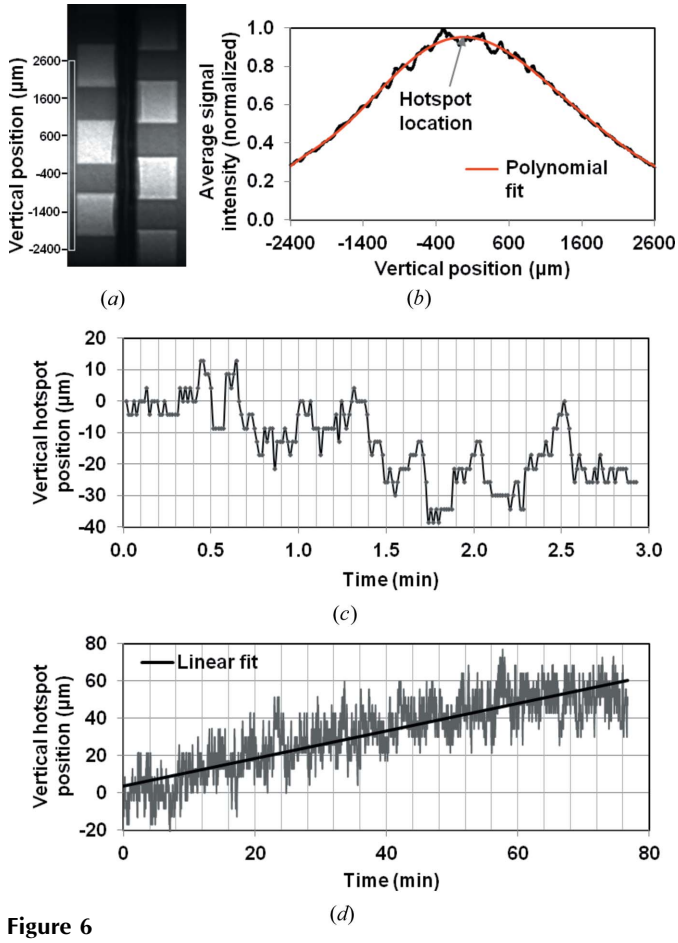

(*a*) (*b*) (*c*) (*d*)

Figure 6
Raw radiograph (*a*) with solid graphite block region (highlighted) used to find the vertical beam intensity profile. Vertical beam intensity profile (black) with eighth-order polynomial fit overlaid in red (*b*). Calculated vertical position of the beam hotspot over 3 min (*c*). Vertical hotspot position *versus* time (*d*) for an extended period (gray), with the linear trend overlaid in black.

No calculation has been made of the loss of spatial resolution due to beam position movement, although such a study would indeed be of interest to the community. However, the effects of the beam position movement can be mitigated using the techniques described in the following sections, thereby decreasing such a loss in resolution.

7. Image analysis with beam position pairing

Under ideal circumstances (no beam-position movement), a single dry-state radiograph could be used to normalize all subsequent wet-state radiographs. When the beam position is not constant, one way to address the problem of false water thickness calculations is to normalize wet-state radiographs to dry-state radiographs obtained at similar beam positions (determined through hotspot tracking, Fig. 6). This beam position pairing approach is possible with a sufficiently large set of dry-state images obtained over a range of beam positions. However, this beam position pairing approach was only possible with experiments that involved a vertically oriented homogeneous region containing the vertical position of the hotspot, free of water during the entirety of the visualization. When this region is not present in the radiograph, a more general method is required to account for beam fluctuations.

A second approach to addressing the problem of false water thickness is to characterize the beam position from the intensity of the false water thickness artefacts when all wet-state radiographs are normalized by a single dry-state radiograph. A quantity entitled 'false water gradient' is employed to quantify the artefact intensity. To illustrate what is meant by the false water gradient, consider Fig. 7(*a*), where an overall vertical gradient is seen in the normalized radiograph, displaying calculated water thickness.

For any subsection of a normalized radiograph, the value for the average vertical gradient of false water thickness can be calculated. Three such subsections are chosen (outlined in Fig. 7*a*), the average value of water thickness *versus* position is calculated (Fig. 7*b*), and the associated vertical water thickness gradient of each region as a function of time is displayed in Fig. 7(*c*). The same 3 min period analysed in Figs. 4(*b*) and 6(*c*) are analysed for this demonstration. After all images are normalized to the first image, a net-positive change in beam position produces a negative vertical water thickness gradient. To illustrate the proportionality of the vertical water thickness gradient and the beam position, the gradient values are overlaid onto the position values in Fig. 7(*c*). As there is a negative coefficient of proportionality between these two properties, the gradient data is displayed on an inverted axis in Fig. 7(*c*). Fig. 7 also demonstrates that the region of interest (ROI) chosen for this analysis can be that of a highly heterogeneous portion of the radiograph, and is not restricted to regions corresponding to homogeneous materials that was described before for the first beam position pair approach. However, as the presence of water may distort the calculated gradient in wet-state radiographs, it is necessary to choose a relatively dry portion of the radiograph as the ROI for gradient calculation. Once each radiograph is characterized in terms of gradient, dry-state radiographs and wet-state radiographs can be paired.

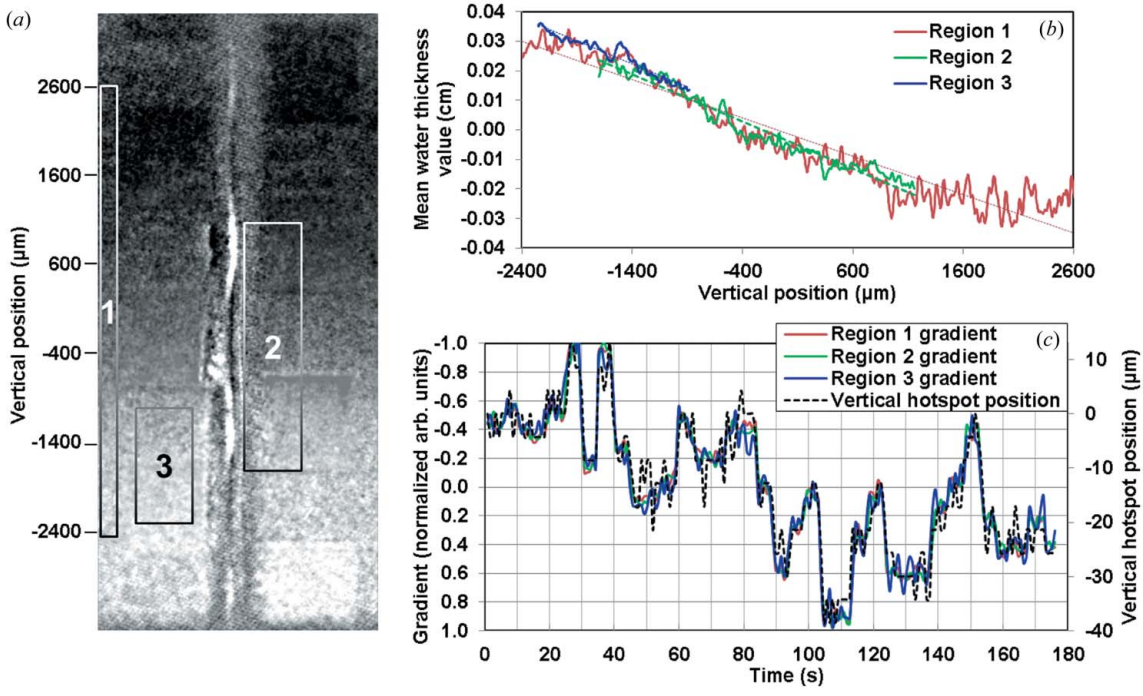

Figure 7
Three regions of a normalized radiograph (*a*) displaying significant false water artefacts. Region 1 is entirely within the solid graphite block. Region 2 samples a heterogeneous region of the radiograph, including rib, channel and GDL. Region 3 samples a region of the radiograph well below the vertical position of the hotspot. The mean water thickness values for each of the three regions (solid lines), with a linear fit (dashed lines) at a single point in time (*b*). Normalized values of the three regions' gradients over 3 min compared with the calculated vertical hotspot position for the same image sequence (*c*).

8. Image processing routine

The following automated processing routine was employed:

(1) Account for the effects of ring current decay on radiograph intensity using equation (5).

(2) Characterize the beam position of each radiograph by calculating false water thickness gradients:

(*a*) Select an ROI for gradient calculations, preferably in the absence of liquid water.

(*b*) Normalize this ROI sequence with the same ROI of a single, arbitrary dry-state radiograph using the Beer–Lambert law.

(*c*) Label each radiograph with the average vertical water thickness gradient calculated from the associated, normalized ROI.

(3) Pair each wet-state radiograph to the dry-state radiograph with the closest corresponding ROI gradient value calculated in step (2). Then, apply the Beer–Lambert law to each wet-state radiograph with the paired dry-state image.

The pairing and normalizing process was automated with a routine written in MATLAB.

To reduce the noise associated with the charge-coupled device (CCD) camera, the above algorithm can be modified to pair the best n dry-state radiographs to a single wet-state radiograph, where n is the number of dry-state radiographs with similar vertical water thickness gradients.

Fig. 8 displays two wet-state radiographs normalized with and without gradient pairing to demonstrate the effectiveness of this technique. Due to the movement of the average hotspot position, it is advisable to obtain dry images at various times throughout experiments since the range of dry hotspot positions should overlap the range of wet hotspot positions.

The primary difference between the processing routine used for this study and a more traditional routine is the selection of an appropriate dry-state radiograph for each individual wet-state radiograph for normalization. Therefore, there is no expected loss of spatial or temporal resolution due to these processing steps. In fact, the resultant spatial resolution is improved when compared with that of a traditional processing routine, where a single dry-state radiograph would be employed to normalize the entire sequence. In a traditional processing routine, the beam positions associated with the majority of wet-state radiographs would be poorly aligned to that of a single dry-state radiograph.

It should be noted that some experimental set-ups allow the capture of a 'bright-field' radiograph, where the sample is moved away from the field of view. This bright field data is then incorporated into the normalization routine. However, for the experiments described in this paper, the apparatus was permanently fixed to the sample stage and a bright-field data sequence could not be captured during the experiment.

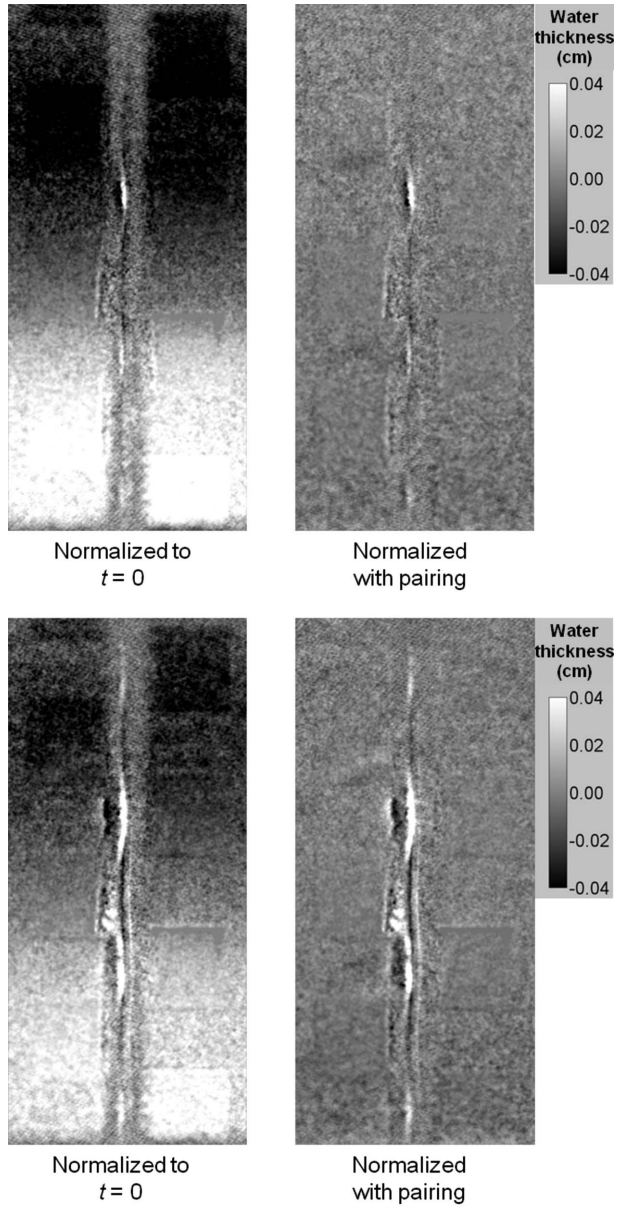

Figure 8
A comparison between radiographs normalized to the dry-state radiograph at $t = 0$ and the same radiographs normalized to the dry-state radiographs with matching false water thickness gradient values. The pairs of radiographs at the top and bottom provide two examples of this comparison.

9. Conclusion

Artefacts resulting from vertical beam position movement were observed upon processing radiographs obtained through synchrotron X-ray radiography. Radiograph sequences captured to identify the dynamic behaviour of liquid water in PEMFC materials were normalized using the Beer–Lambert law. Upon tracking the vertical beam position, it was determined that small oscillations of beam position were present with an amplitude of $\sim$25 µm and a frequency of $\sim$50 mHz. In addition, the mean beam position was observed to move vertically at a speed of 0.74 µm min^{-1}. It was determined that small changes in beam position, measuring 25 µm, could result in a 'false water' signal representing up to $\pm$350 µm of water thickness.

The vertical gradient of this false water artefact was employed to characterize the beam position of each radiograph in the sequence. Then, instead of normalizing all wet-

state radiographs against a single dry-state radiograph, dry-state and wet-state radiographs were paired with respect to this gradient. This technique is shown to mitigate artefacts associated with beam position movement without causing any loss of temporal or spatial resolution, but requires a sequence of dry radiographs with beam positions that sufficiently overlap the beam positions of the wet radiographs.

The authors would like to acknowledge the generous assistance of Dr George Belev and Dr Tomasz Wysokinski at the Canadian Light Source, in Saskatoon, SK, Canada. The authors would also like to thank Mr Jongmin Lee, at the MESTP Laboratory, University of Toronto, for his help while collecting the data at the Canadian Light Source Inc., Saskatoon, SK. Research described in this paper was performed at the Canadian Light Source Inc., which is supported by the Natural Sciences and Engineering Research Council of Canada, the National Research Council Canada, the Canadian Institutes of Health Research, the Province of Saskatchewan, Western Economic Diversification Canada, and the University of Saskatchewan. Financial support to the authors from The Natural Sciences and Engineering Research Council of Canada (NSERC), Bullitt Foundation, Canada Foundation for Innovation (CFI), the Hatch Scholarship for Sustainable Energy Research, and University of Toronto are also gratefully acknowledged.

References

Bazylak, A. (2009). *Int. J. Hydrogen Energy*, **34**, 3845–3857.
Belev, G., Wysokinski, T. W., Chapman, D., Mullin, C. & McKibben, M. (2011). *Nucl. Instrum. Methods Phys. Res. A*, **649**, 225–227.
Chattopadhyay, S. (1990). *Nucl. Instrum. Methods Phys. Res. A*, **291**, 455–460.
Chumakov, A., Rüffer, R., Leupold, O., Celse, J.-P., Martel, K., Rossat, M. & Lee, W.-K. (2004). *J. Synchrotron Rad.* **11**, 132–141.
Dalzel, M. (2010). Canadian Light Source Research Report. CLS, Saskatoon, Canada.
Hartnig, C. & Manke, I. (2009). *Encyclopedia of Electrochemical Power Sources*, pp. 738–757. Amsterdam: Elsevier.
Hartnig, C., Manke, I., Kuhn, R., Kleinau, S., Goebbels, J. & Banhart, J. (2009). *J. Power Sources*, **188**, 468–474.
Krüger, P., Markötter, H., Haußmann, J., Klages, M., Arlt, T., Banhart, J., Hartnig, C., Manke, I. & Scholta, J. (2011). *J. Power Sources*, **196**, 5250–5255.
Kuhn, R., Scholta, J., Krüger, P., Hartnig, C., Lehnert, W., Arlt, T. & Manke, I. (2011). *J. Power Sources*, **196**, 5231–5239.
Lee, S., Kim, S., Park, G. & Kim, C. (2010). *Int. J. Hydrogen Energy*, **35**, 10457–10463.
Leonard, G., Nurizzo, D., Mueller-Dieckmann, C., Mitchell, E., McCarthy, J., Flot, D., Bento, I. & Lindley, P. (2008). *Astrophysics and Condensed Matter, Horizons in World Physics*, Vol. 262, p. 269. New York: Nova Science Publishers.
Maier, W., Arlt, T., Wannek, C., Manke, I., Riesemeier, H., Krüger, P., Scholta, J., Lehnert, W., Banhart, J. & Stolten, D. (2010). *Electrochem. Commun.* **12**, 1436–1438.
Manke, I., Hartnig, C., Gruenerbel, M., Lehnert, W., Kardjilov, N., Haibel, A., Hilger, A., Riesemeier, H. & Banhart, J. (2007). *Appl. Phys. Lett.* **90**, 174105.
Markoetter, H., Manke, I., Krueger, P., Arlt, T., Haussmann, J., Klages, M., Riesemeier, H., Hartnig, C., Scholta, J. & Banhart, J. (2011). *Electrochem. Commun.* **13**, 1001–1004.
Proux, O., Nassif, V., Prat, A., Ulrich, O., Lahera, E., Biquard, X., Menthonnex, J.-J. & Hazemann, J.-L. (2006). *J. Synchrotron Rad.* **13**, 59–68.
Schneider, A., Wieser, C., Roth, J. & Helfen, L. (2010). *J. Power Sources*, **195**, 6349–6355.
Wysokinski, T. W., Chapman, D., Adams, G., Renier, M., Suortti, P. & Thomlinson, W. (2007). *Nucl. Instrum. Methods Phys. Res. A*, **582**, 73–76.